Experimental and Finite Element Simulation for Thermal Distribution in TIG, MIG and TIG-MIG hybrid welds

Cynthia Samuel Abima[a], Nkosinathi Madushele[a], Fredrick Madaraka Mwema[a,] Stephen Akinwale Akinlabi[b]
*oyamacynthia@gmail.com, nmadushelee@uj.ac.za, fredrick.mwema@dkut.ac.ke, stephen.akinlabim@northumbria,
[a] Mechanical Engineering Science, University of Johannesburg, Johannesburg, South Africa.
[b] Mechanical Engineering and Construction Engineering, Northumbria University, United Kingdom

Abstract:

The Tungsten Inert Gas-Metal Inert Gas (TIG-MIG) hybrid process has the combined advantages of standalone TIG and MIG welding processes. This study investigates the thermal distribution of the TIG-MIG hybrid welding process compared to the standalone TIG and MIG welding processes. The welds' mechanical properties, microstructural evolution, and phase formation are also discussed. The process parameters for the TIG-MIG, TIG and MIG welding processes used in this study were obtained from prior parametric optimisation for each welding process performed by the Taguchi method with an L-9 orthogonal matrix. The thermal behaviour of TIG, MIG and TIG-MIG welds were investigated by adopting the Gaussian heat source model on the ANSYS workbench. The simulated temperature distributions of the three weld types were validated by the mechanical, microstructural, and phase formation characteristics as obtained experimentally. Similar temperature profiles were observed for all weld types having peak temperatures at the weld seams. The simulated temperature distributions were in good correlation with the experimentally obtained from the hardness results, microstructural evolution and phase formation, as revealed from the X-ray diffraction analysis. Hence, the Gaussian heat source model can accurately simulate the properties of a complex heat source interaction, allowing for process optimisation and forecasting.

Keywords: Hardness, Heat input, MIG welding, Microstructure, Thermal distribution TIG welding, TIG-MIG hybrid welding.

1.0 Introduction

Several advanced welding techniques have emerged to increase weld quality and productivity. The most recent of these technologies is the hybrid welding processes introduced to improve joint penetration, modify welds microstructures, and improve mechanical properties [1]. Hybrid welding describes welding processes which combine two or more heat sources to achieve a single weld bead. Since its introduction, various hybrid welding processes have been adopted, including the Tungsten Inert Gas-Metal Inert Gas (TIG-MIG), Laser-MIG, Laser-TIG, Plasma-TIG, and TIG-Friction stir welding. Among these, the Tungsten Inert Gas-Metal Inert Gas (TIG-MIG) hybrid welding process, introduced for achieving deeper penetration joints, especially for thick members and dissimilar metal joining, is preferred for industrial welding due to its relatively cheaper cost and ease of operation. Another selling point for the TIG-MIG process is the fact that hybrid weldings that combine the laser heat source are very expensive and require a huge manpower training. The TIG-MIG welding technique combines the advantages of individual welding processes and minimises their respective limitations [2], [3]. Following this, many studies have recorded improved mechanical and microstructural properties with the TIG-MIG hybrid process through experimental characterisations. For

example, Cheng et al. [4] achieved an excellent joint void of cracks and pores on dissimilar copper/stainless joint via the TIG-MIG hybrid process. The authors reported homogeneous composition in the weld zone, which they attributed to the low heat input during welding. Likewise, Abima et al. [5] compared the mechanical and microstructural properties of the TIG-MIG hybrid joint with standalone TIG and MIG welding processes. Their result shows that the hybrid joints have higher yield strength, tensile, and percentage elongation than standalone TIG and MIG processes. The hybrid welded joint had the lowest hardness value, attributed to the large presence of iron phases. Somani and Lalwani [6] affirm that the ultimate tensile strength of austenitic steel welded via TIG-MIG welding was higher than that obtained from the parent material. Desirable ferrite and vermicular microstructure were also achieved.

The dual heat used in TIG-MIG hybrid welding makes understanding the mechanisms of the thermal distribution and weld pool and droplet behaviour very challenging. Consequently, researchers began adopting the numerical and finite element method to study these behaviours by mimicking the physical system. Such methods include a moving heat source in a quasi-stationary state proposed by Rosenthal [7], Gaussian distribution recommended by Pavelec et al. [8] and the ellipsoidal heat source model introduced by Doldak et al. [9]. These mathematical models, along with a few others, have reportedly been found to be reliable at forecasting weld characteristics. For instance, by adopting the constant heat flux model, Vemanaboina et al. [3] simulated the thermal distribution and residual stresses upon TIG welding of 304 steel. The authors observed that the fusion zone had a greater temperature field and residual stresses than the HAZ and the parent material at constant heat flux. Likewise, Sun et al. [10] adopted a combined heat source model to investigate the temperature fields in the VPPA-GMAW and to simulate the weld geometries. Their work showed that experimentally obtained weld geometries were in good agreement with the simulated geometry. Venkateswarlu et al. [11] adopted Goldak's single ellipsoidal heat source to investigate the temperature distribution in MIG welding of dissimilar IS2062 steel and Inconel on ANSYS APDL software. The authors reported effective movement of the heat source on account of elliptical temperature contours. Additionally, Wu et al. [12] studied the influence of welding speed, TIG current and distance between electrodes on the weld pool behaviour of TIG-MIG hybrid welded Q235. They evaluated the temperature field, heat flux and fluid flow as it affects the weld pool behaviour. The authors observed that an increase in TIG current increases the heat flux. Also, filling the weld toe becomes challenging when the welding speed goes beyond 2.0m/mm, and the velocity of the droplet becomes larger as the distance between electrodes increases. Kumar et al. [13] investigated the effect of TIG welding current on the thermal distribution, microstructural and mechanical properties of 304L steel. The authors reported a sharp decrease in temperature at a location adjacent to the weld centre. This behaviour was attributed to the nonlinear variation in the thermo-physical temperature-dependent material properties. The reverse was the case for ultimate tensile strength and percentage elongation, which showed a corresponding increase as the welding current increased. Another author, Ebrahimpour et al. [14], investigated the effect of torch angle and TIG arc on TIG-MIG welded 2205 duplex steel via experimental and finite element methods. Their result from both methods showed that a leading TIG arc increases the maximum temperature of the welds. Zong et al. [15] also studied the droplet transfer and arc shape characteristics to investigate the heat and force distribution in TIG-MIG and TIG weld pool of 0.17% carbon mild steel plate. A thick liquid metal with a slightly lower cooling rate was observed at the rear and middle of the weld pool, while a leading MIG arc suppressed undercut defects in TIG-MIG hybrid welding. Also, the MIG arc increases as the TIG current increases, thus lowering the heat flux in TIG-MIG welding as opposed to conventional MIG welding. Zubairuddin et al. [16], where the Goldak's heat source model was used to simulate the weld properties in MIG welded of chromium reach

steel on Sysweld software. The thermal cycle simulated was in good agreement with the microstructural evolution from experimental characterisation. Also, Chen et al. [17] simulated the thermo-plastic behaviour of 316 steel in laser-arc welding. The outcome of their simulation was validated by the experimental microstructure, hardness and XRD analysis. The authors recorded a close range between the simulated and experimental results

Literature reveals that a few studies investigate the thermal distribution of the MIG, TIG and TIG-MIG hybrid welding processes even though it plays a key role in the microstructural orientation and evolution. There is a lack of fundamental research to understand the transient thermal distribution in the TIG-MIG hybrid of AISI 1008, which is the most commonly used industrial steel for numerous fabrication and construction processes due to the double heat source and numerous interactions of process parameters. Hence more investigation into the thermal behaviour of MIG, TIG and TIG-MIG hybrid welded AISI 1008 mild steel is needed.

This work reports the experimental and finite element simulation for thermal distribution in TIG, MIG and TIG-MIG hybrid welds. The hardness, microstructural properties and phase formation in the welded joints were obtained via experimental characterisations and were used to validate the simulated thermal behaviour of the respective joints. This section presents a background to existing works and highlights the focus of this study. Section 2 will show the study's methodology, while section 3 presents the results and findings from the numerical and experimental works. Lastly, the conclusion is presented in section 4.

2.0 Materials and Procedures

2.1 Materials

The choice base material for this study is AISI 1008 mild steel with plate dimensions of 100 mm x 100 mm x 6 mm. A 2.4 mm diameter ER70S/6 carbon filler was used. ER70S/6 filler wire is the most suitable wire for mild steel and low alloys steel [18]. Moreso, its selection was influenced by its high deoxidation properties and good hardness, tensile and yield strength properties in its as-welded condition [19], [20]. The butt joint configuration maintained a root gap of 2.5 mm between the plates. The chemical composition by weight of the base material and ER70S/6 are Fe - 99.58, C - 0.079, S - 0.0098, Mn - 0.32, P - 0.0098 and C- 0.06-0.15max, Ni -0.15, Mn 1.4, Si-0.8-1.15 max, S -0.035, V-0.03max Mo-0.15max respectively. The mechanical properties of the is presented in Table 1.

Table 1. Mechanical properties of base metal – AISI 1008

Property	**Metric Value**
Tensile strength	340 MPa
Yield strength (depending on temper)	285 MPa
Elastic modulus	190-210 Gpa
Bulk modulus (typical for steel)	200 GPa
Shear modulus (typical for steel)	80.0 GPa
Poisson's ratio	0.30
Elongation at break (in 50 mm)	20%
Reduction of area	45%

2.2 Experimental procedures and process parameter

Three different welding techniques (the TIG, MIG, and the TIG-MIG hybrid) were used to produce respective joints. The welding direction of all welds follows the rolled direction of the plates. In the hybrid welding, the TIG torch was set as the leading torch, followed by the MIG torch, while individual welds were produced for the MIG and TIG welding processes respectively. A schematic representation of the TIG-MIG hybrid process is presented in Figure 1.

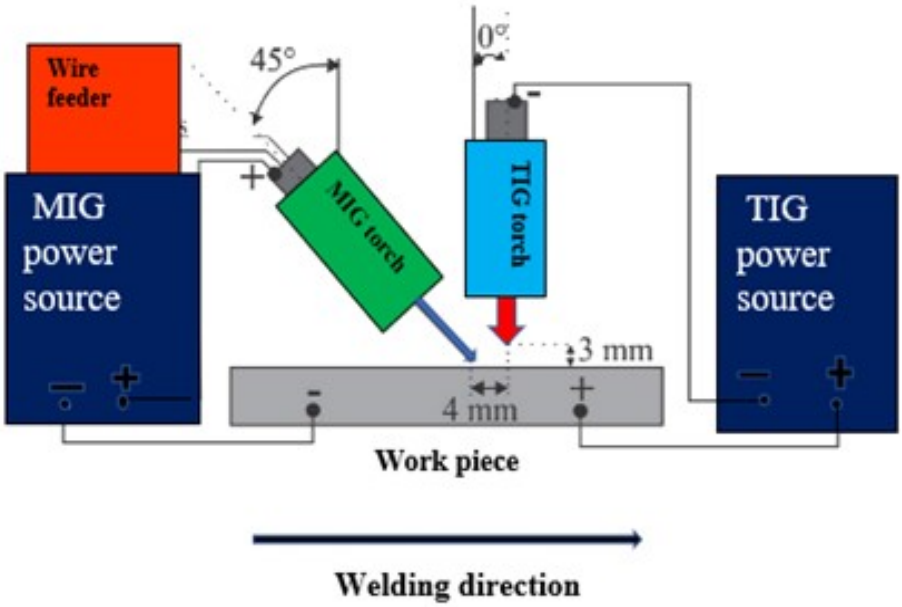

Figure 1. TIG-MIG welding schematic representation [5]

Following the completion of welding, test specimens for microhardness, microstructural, and X-ray diffraction (XRD) investigation were cut from the welded plate. The welding voltage, current and gas flow rate were the choice process parameters for the welding operation. The values of input parameters employed were obtained from prior parametric optimisations targeted at the highest tensile strength based on the Taguchi L-9 orthogonal matrix for each weld type. The process parameters used in this study is presented in Table 2.

2.3 Numerical procedures

As in the physical experiment, the precise geometry and setup were replicated in the models for the transient simulation of the TIG, MIG, and TIG-MIG processes and modelled using the ANSYS Spaceclaim design platform. The weld parameter specifications for the three weld types are presented in Table 2.

Table 2: Weld parameter specifications (TIG, MIG and TIG-MIG welding processes)

Process Parameter	TIG Weld	MIG Weld	Hybrid weld	
			TIG pass	MIG pass
Heat input (W)	3780	675.4	3780	750.75
Welding Time (S)	200	10	200	15
Weld velocity (mm/s)	0.5	10	0.5	6.67
Arc Radius	5 mm	3 mm	5 mm	3 mm
Welding Voltage	15 V	30 V	15 V	30 V
Welding Current	180 A	280A	180 A	280 A

Gas Flow Rate	15 L/mm	17 L/mm	15 L/mm	17 L/mm

In order to depict the transport of heat from the weld pool to the remaining portion of the material, the conduction heat transfer equation was used. The convective boundary heat transfer equation was used to describe how air molecules travel across the material surface, transferring heat from the base material to the surrounding environment. This study assumes a pronounced heat transfer occurrence at the surface boundaries compared to the interior portions of the metal. The ADPL solver accounts for boundary convection by iteratively calculating the difference between the base material temperature and the surrounding air temperature and then multiplying it by the two bodies' respective heat transfer coefficients. Lastly, radiation boundary heat transfer was applied as described by Stefan Boltzmann's law. These governing equations are represented in Equations 1,2,3, respectively.

$$k_x \frac{\delta^2 T}{\delta x^2} + k_y \frac{\delta^2 T}{\delta y^2} + k_z \frac{\delta^2 T}{\delta z^2} + \rho Q = \rho C_T \frac{\delta T}{\delta t} \qquad (1)$$

Where ρ = density of the base material, C_T =specific heat capacity and Q = internal heat generation rate.

$$q_{con} = h_f(T - T_\infty) \qquad (2)$$

Where q_{con} =heat transfer due to convention (W/m^2), h_f = heat transfer coefficient $(W/m^2°C)$, T= temperature (°C), T_∞ Ambient temperature (°C)

$$q_{rad} = \sigma\varepsilon(T^4 - T_\infty^4) \qquad (3)$$

Where $\varepsilon = Emmisivity\ of\ the\ material, \sigma = Stefan - Boltzmann's\ Constant,\ T = body\ temperature, T_\infty = ambient\ temperature$

A coupled radiative and convective heat transfer condition were used to model losses at the boundaries of the material, between the surface and the ambient. The material is assumed to have a thermal emissivity of 0.9 and is assumed to be placed in still air with an ambient temperature of 27 degrees Celsius. The overall heat transfer coefficient between the surface of the material and the ambient is $5w/mm^2$.

2.3 Heat Source Modelling

The Gaussian heat source model is adopted to simulate the temperature distribution in this study. The plate thickness has made the 2-dimensional surface heat source model sufficient to depict the heat distribution on the material accurately.

Due to the thickness of the weld plates, the 2-dimensional surface heat source model can the heat load distribution on the material. A three-dimensional technique might be necessary to maintain accuracy during the simulation for thicker plates. The Gaussian heat source model is mathematically represented by Equation 4. The Gaussian heat source model is presented in Figure 2.

$$q(r) = \frac{\eta UI}{2\pi r_o^2} \exp\left[\left(\frac{r^2}{2r_o^2}\right)\right] \qquad (4)$$

Where $r_0 = Effective\ radius\ of\ the\ welding\ arc,\ q(r) = Rate\ of\ heat\ input\ (W)$, U = welding voltage I= welding current, r = the radial position from the centre of the arc η = thermal efficiency of the welding process, usually given as 0.7 and 0.8 for TIG and MIG, respectively.

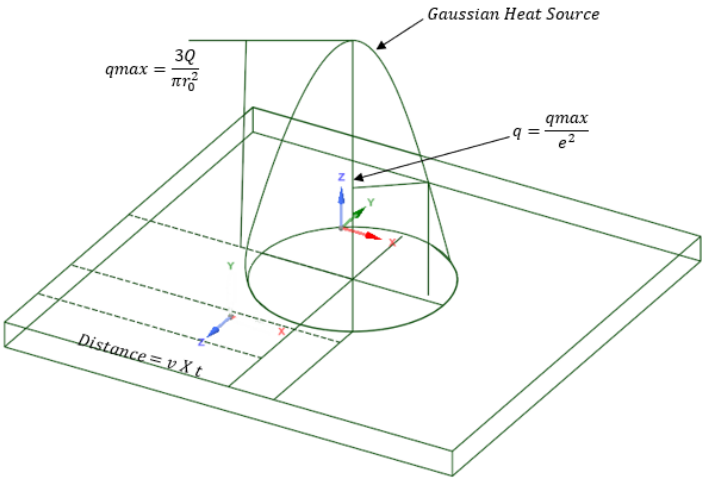

Figure 2. Sketch showing the Gaussian heat source model

2.4 The Meshing of Geometry

The ANSYS ICEM platform created a fine mesh for numerical computing with a total of 68883 nodes and 13208 components. Along the weld seam, additional elements were added to assure great precision. The mesh density was maintained at a level that would guarantee accurate and convergent solutions. Similar approach was adopted by [1] and Mishra It was observed that further meshing did not enhance the solution's accuracy, leading to the conclusion that the mesh density and refinement obtained were optimal for the numerical computation of the welding processes. The temperature-dependent characteristics of AISI 1008 mild steel, the filler material, and the base metal's thermophysical qualities described by Brown and Song [21] and Mahapatra et al. [22] were keyed into the simulation process to specify the mechanical and thermal properties of the model studied. A representation of the generated mesh is presented in Figure 3.

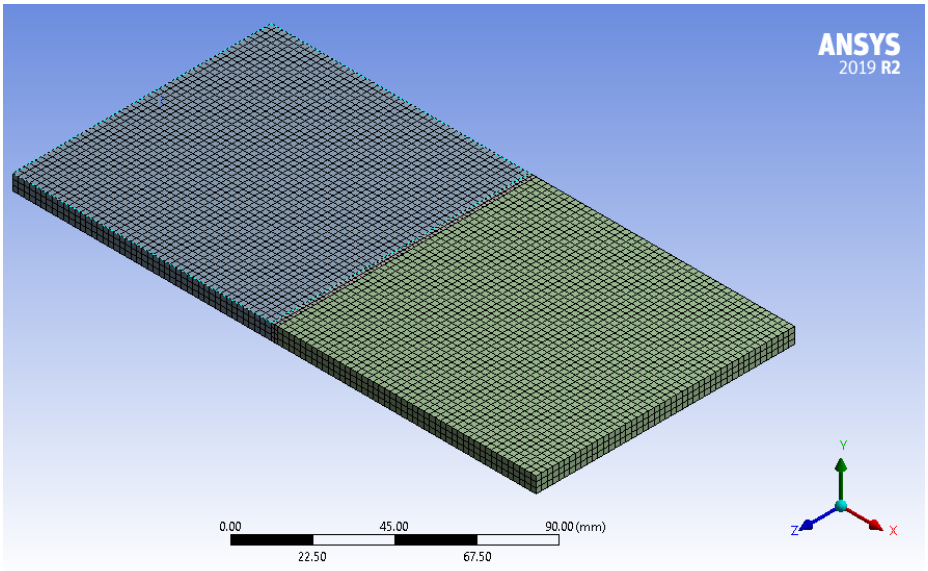

Figure 3. Mesh generated for the simulation model

3.0 Results and Discussions

3.1 Hardness Results

The Vickers microhardness testing machine with a force of 300N was used to measure the welds' hardness across the transverse section as per ASTM E384 [23] testing standard. A dwell time of 15 seconds was maintained for all tested samples. The average hardness values obtained in the fusion zones of the TIG, MIG and TIG-MIG welds are 227.4 HV, 211.4 HV and 176.3 HV, respectively. The average hardness values obtained for the HAZ are 154.8 HV, 143.0 HV, and 142.3 HV. These figures clearly show that the fusion zones had higher values compared to the HAZs of all weld types. This result is similar to the report recorded by Lee et al. [24]. The results also show that the TIG welded joint had the highest hardness values in both FZ and HAZ, followed by the MIG weld, while the TIG-MIG weld had the lowest hardness value. A similar hardness trend was observed in the HAZs.

3.2 Microstructural Evaluation

This section discusses the experimental microstructural characterisation of the welded samples for the three weld types. Only microstructural behaviour in the fusion zone (FZ) and the heat-affected zones (HAZs) are considered in this study. The TIG microstructure is mainly characterised by the presence of acicular ferrites structures. Finer acicular ferrites were observed in the fusion zone than in the HAZ. The fusion zone of the MIG welded joint is characterised by a few fine acicular ferrites and large widmanstatten structures. Sahasrabudhe and Raut [25] reported similar stuctures. MIG weld HAZ exhibited coarse ferrite grains and randomly distributed cementite. The fusion zone of the TIG-MIG weld was characterised by a large presence of clustered pearlite and re-crystalline ferrites grains. In contrast, the HAZ exhibited coarse dendritic pearlite structures with large ferrites grains. The microstructures of the fusion zone and the heat-affected zones for the TIG, MIG and TIG-MIG hybrid welds are presented in Figure 4.

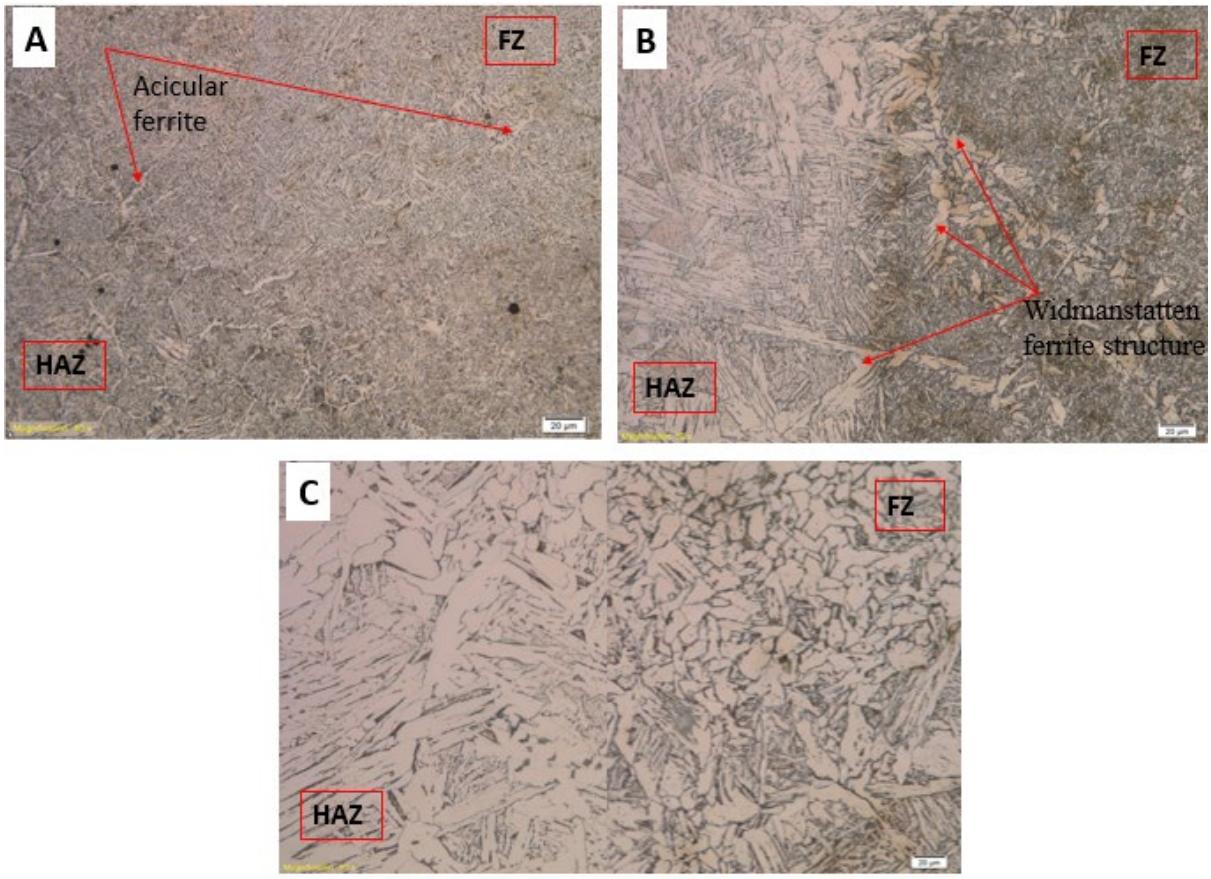

Figure 4. Microstructure evaluation (A) TIG weld (B) MIG weld (C) TIG-MIG weld

3.3 X-ray Diffraction Analysis

The x-ray diffraction analysis for the three weld types are presented in 5. The diffractogram of the TIG joint shows high peak intensities of martensite phases and little iron (Fe) peak diffracting at 43.76º. The MIG welded joint's diffractogram exhibits more iron phases at high peak intensities 45.38º and 83.07º. Finally, only iron phases were visible in the TIG-MIG welded joint. The XRD reaults validate the hardness results as martensite structures are known to improve hardness [26].

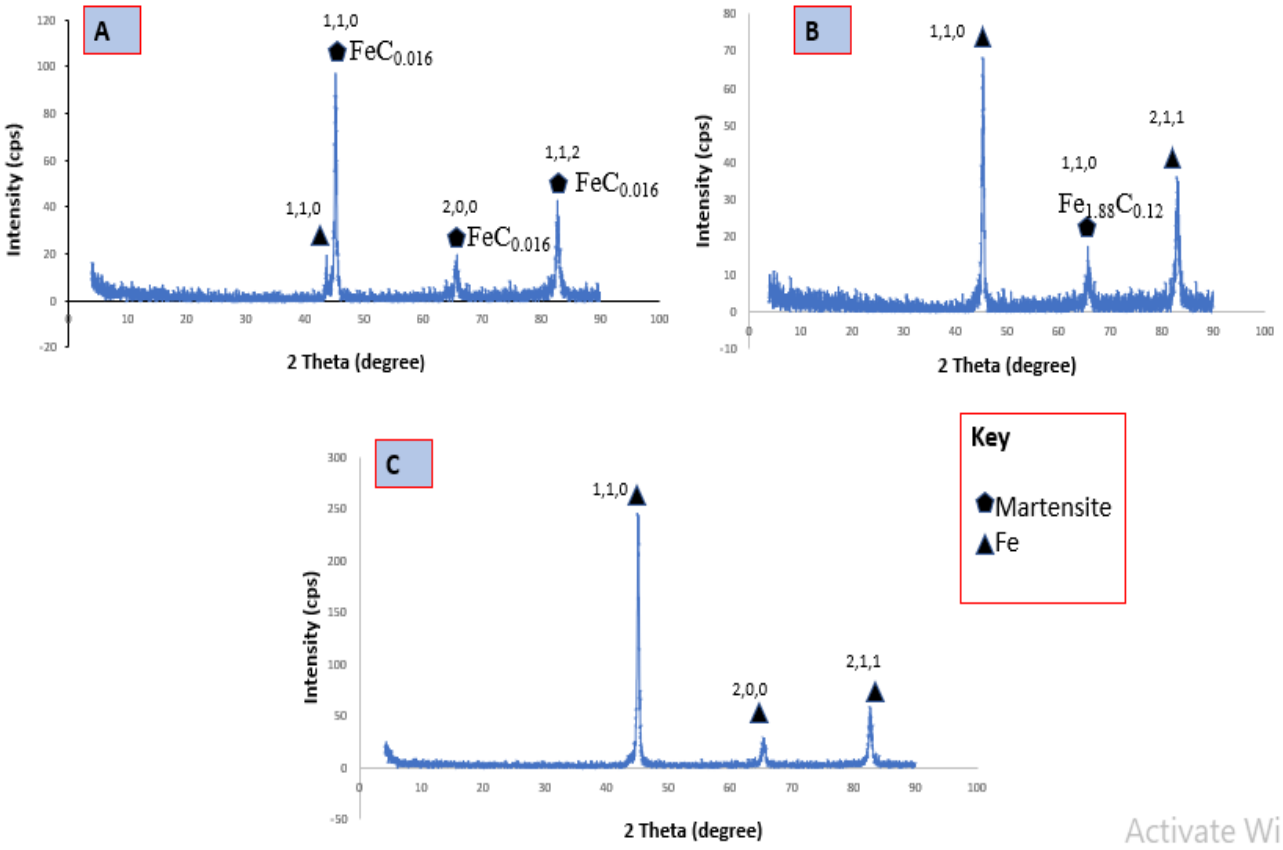

Figure 5. Diffractogram (A) TIG weld (B) MIG weld (C) TIG-MIG weld

3.4 Numerical thermal Distribution

Transient thermal temperature distribution across the weld zones was achieved by inserting temperature probes at precise intervals beginning at the weld seam during the simulation process. For lack of experimental temperature measurement, the simulated temperature distributions for the three welding processes were validated against the microstructural evolution, the hardness and the XRD results from the experimental outcome. The highest temperatures were recorded at the fusion zones for all weld types. The temperature distribution patterns also showed symmetricity about the weld seam due to the similarities between the material properties of the two weld plates. The transient simulation of the TIG, MIG and TIG-MIG welding process ran according to the time specifications presented in Table 2. The temperature distribution was recorded for all welds at 5 mm, 10 mm, 15 mm, and 20 mm away from the weld centre.

The higher temperature gradient in the weld seam (fusion zone) resulted in a higher cooling rate for the TIG weld. The fast cooling rate in this region resulted in finer ferrite, acicular ferrite grain structures and the martensite phase, as revealed by microstructure and the XRD analysis as presented in Figure 4 and Figure 5, respectively. This explained the higher hardness properties of the TIG weld. A similar observation was reported by Yazdian et al. [27], [28]. Whereas at 5 mm away from the weld seam (HAZ), a lower temperature gradient leads to a slower cooling rate, resulting in a coarse grain structure of acicular structures. At 10 mm and further, the material is not heated above 500 ºC and is only tempered. The temperature-time graph is presented in Figure 6, while Figure 7 shows the temperature distribution at 21 seconds, 72 seconds and 200 seconds, respectively.

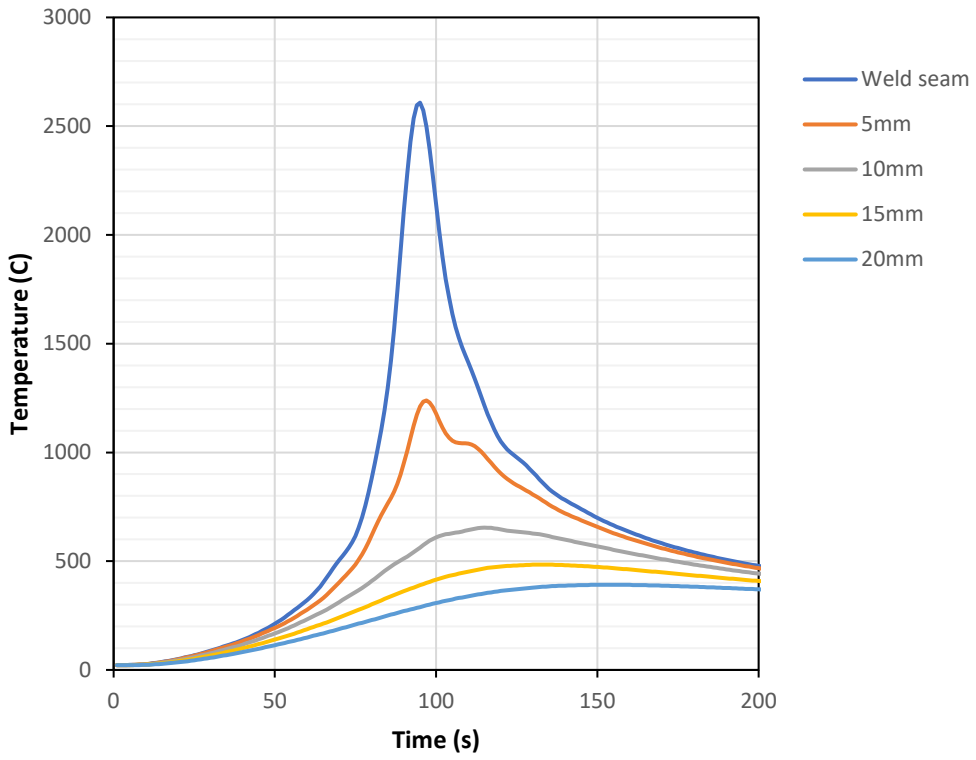

Figure 6. TIG-Temperature-time graph are various distances away from weld seam

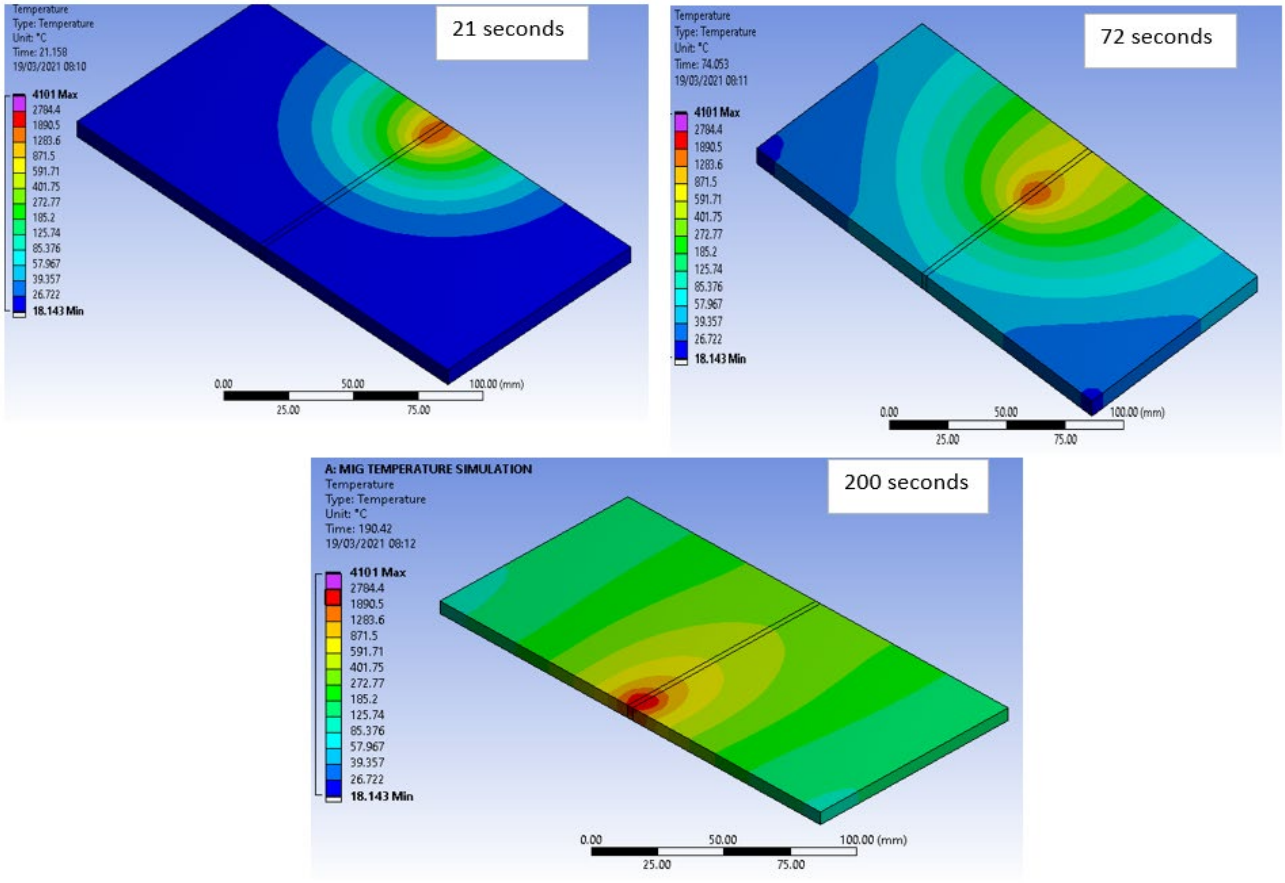

Figure 7. TIG-Temperature distribution along the weld plate during TIG weld simulation

The MIG's temperature distribution pattern was identical to that of the TIG weld. However, the peak temperature was lower than that of TIG. Consequently, the temperature and gradient in the weld seam and at 5 mm away from the seam followed suit. The fusion zone of the MIG weld cooled from above 2367 ºC to 500 ºC leading to widmanstatten ferrite formation, as seen in Figure 4 (B). At 5 mm, a slow cooling curve was observed, which allowed for the formation of ferrite grains and pearlite phases, also visible in Figure 4 (B). The presence of martensite in the MIG weld also contributed to higher hardness compared to the TIG-MIG process and seen from the hardness results. The temperature-time graph and temperature distribution graph during MIG weld simulation is presented in 8 and 9.

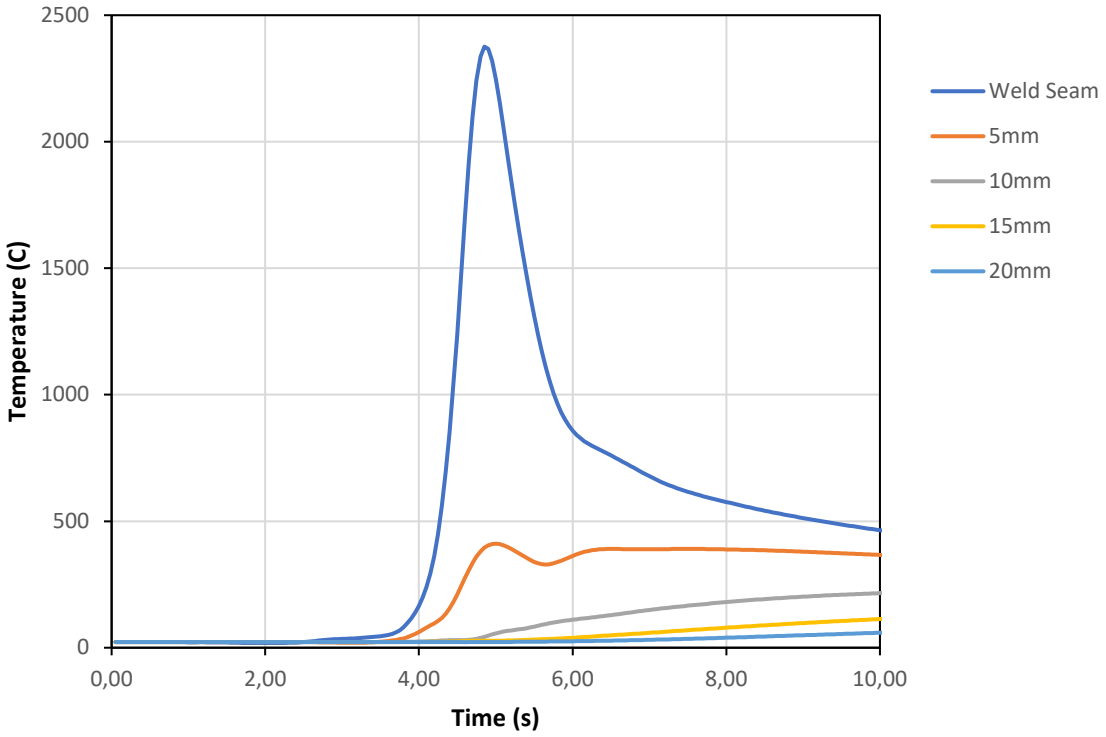

Figure 8. MIG - Temperature time graph are various distances away from weld seam

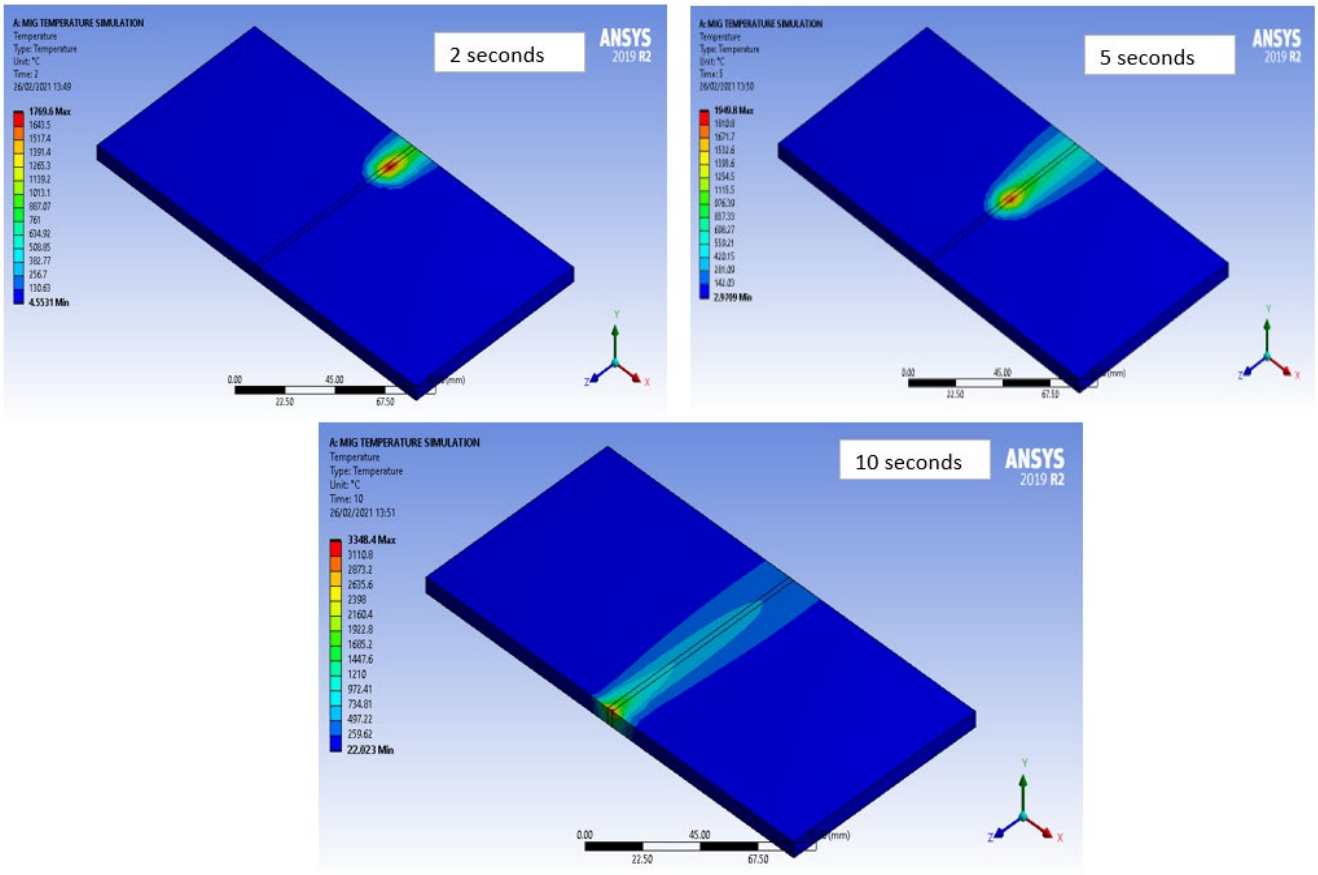

Figure 9. MIG- Temperature distribution along the weld plate during TIG weld simulation

The simulated temperature gradient for the TIG-MIG process shows a very high peak temperature, which is attributed to the high heat input and a gentle gradient. The gentle slope at the weld seam and HAZ led to the slow cooling rate. The double heat input and slow cooling rate allowed for re-heated ferrites grains and the formation of pearlite structures in the fusion zone. The HAZ exhibited coarse dendritic pearlite structures with large ferrites grains, which also resulted in lower hardness values in this region. A similar account was reported by Loureiro Altino [29]. The lower hardness is also attributed to the presence of only iron (Fe) phases, as revealed in Figure 4(C). Figure 10 shows the temperature-time graph while the temperature distribution during TIG-MIG weld simulation at times (t) = (a) 5 seconds, (b) 10 seconds (c) 15 seconds is presented in Figure 11.

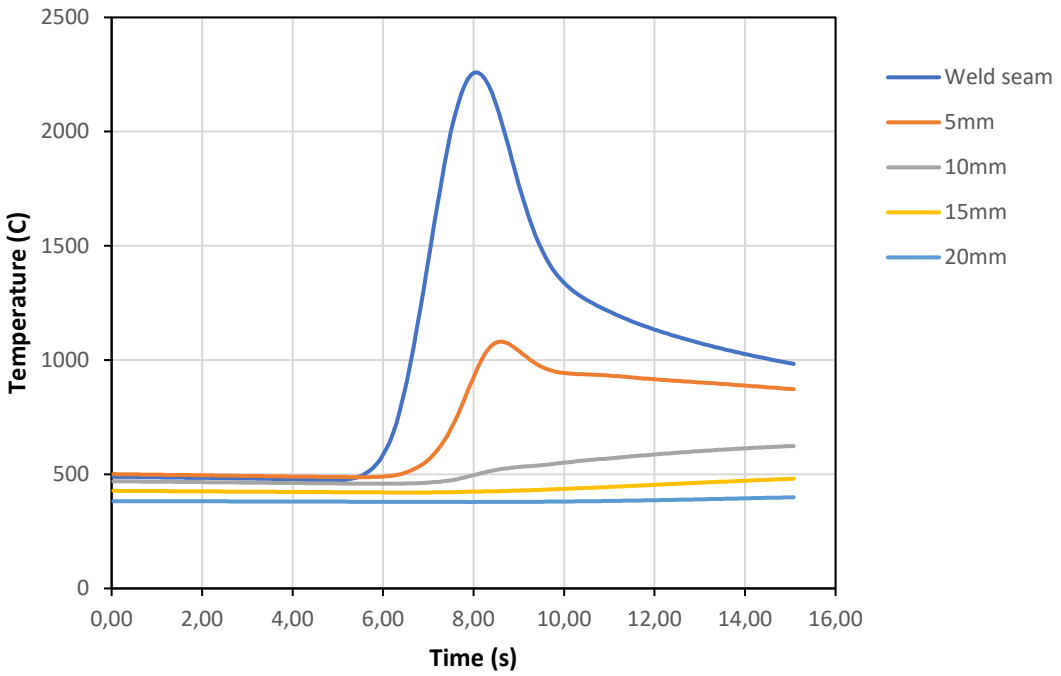

Figure 10. TIG -MIG - Temperature time graph are various distances away from weld seam

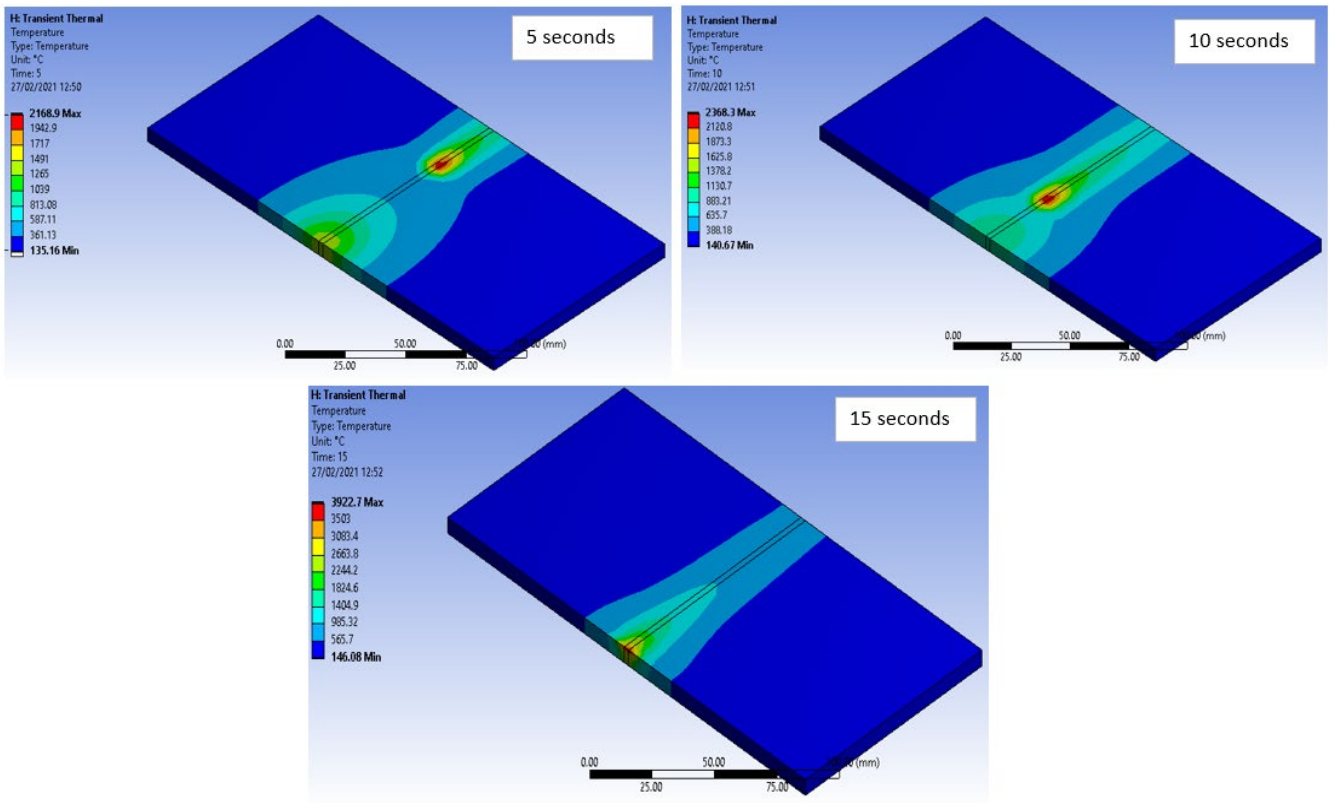

Figure 11. TIG-MIG- Temperature distribution along the weld plate during TIG weld simulation

Conclusion

The finite element simulation of the temperature distribution in TIG, MIG and TIG-MIG hybrid welding of AISI 1008 on the ANSYS workbench have been discussed. The experimental hardness properties, microstructural evolution and phase formation were used to validate the simulated results. The following conclusions can be drawn from this study.

(i) The transient thermal simulations for temperature distribution across the weld zones during the welding processes were in accordance with the physical systems' observations, as the fusion zones exhibited a higher temperature gradient similar to the experimental welding process.
(ii) The simulated temperature distributions were in good agreement with the experimentally obtained hardness values, microstructural evolution and phase formation.
(iii) The TIG-MIG hybrid weld had the least hardness properties due to the presence of only iron phases.
(iv) Martensite formation in the TIG and MIG welded joints resulted to higher hardnes values of the welds.
(v) The Gaussian heat source model can accurately simulate complex heat source interaction properties, allowing for process optimisation and forecasting.

Reference

[1] H. Mehdi, "Influence of Friction Stir Processing on Weld Temperature Distribution and Mechanical Properties of TIG-Welded Joint of AA6061 and AA7075," vol. 73, pp. 1773–1788, 2020.

[2] C. S. Abima, "TIG & MIG Hybrid Welded Steel Joint : A Review," 2019.

[3] C. S. Abima, S. A. Akinlabi, N. Madushele, O. S. Fatoba, and E. T. Akinlabi, "Multi-objective optimization of process parameters in TIG-MIG welded AISI 1008 steel for improved structural integrity," *Int. J. Adv. Manuf. Technol.*, no. https://doi.org/10.1007/s00170-021-08181-1, 2021, doi: 10.1007/s00170-021-08181-1.

[4] Z. Cheng, J. Huang, Z. Ye, Y. Chen, J. Yang, and S. Chen, "Microstructures and mechanical properties of copper-stainless steel butt-welded joints by MIG-TIG double-sided arc welding," *J. Mater. Process. Technol.*, vol. 265, pp. 87–98, 2019, doi: 10.1016/j.jmatprotec.2018.10.007.

[5] C. S. Abima, S. A. Akinlabi, N. Madushele, and E. T. Akinlabi, "Comparative study between TIG-MIG Hybrid, TIG and MIG welding of 1008 steel joints for enhanced structural integrity," *Sci. African*, vol. 17, pp. 1–11, 2022, doi: 10.1016/j.sciaf.2022.e01329.

[6] C. A. Somani and D. . Lalwani, "Experimental study of some mechanical and metallurgical properties of TIG-MIG hybrid welded austenitic stainless steel plates," *Mater. Today Proc.*, vol. 26, pp. 644–648, 2020.

[7] D. Rosenthal, "Mathematical theory of heat distribution during welding and cutting," *Weld. J.*, vol. 20, no. 5, pp. 220–234, 1941.

[8] V. Pavelec, R. Tanbakuchi, O. . Uyehera, and P. Myers, "No Title," *Weld. J. Res.Suppl.*,

pp. 295–305, 1969.

[9] J. Goldak, A. Chakravarti, and M. Bibby, “A new finite element model for welding heat source,” *Metall. Trans. B*, vol. 15 B, pp. 299–305, 1984.

[10] Z. Sun, Y. Han, M. Du, J. Tong, and H. Hong, “An improved simulation of temperature field in VPPA–GMAW of Al–Cu–Mg alloy,” *J. Mater. Process. Technol.*, vol. 263, no. August 2018, pp. 366–373, 2019, doi: 10.1016/j.jmatprotec.2018.08.017.

[11] K. Venkateswarlu, P. N. Kumar, and P. S. Ravikumar, “Finite Element Simulation of Temperature Distribution, Distortion and Residual Stresses of Dissimilar Welded Joints,” *Mater. Today Proc.*, vol. 5, no. 5, pp. 11933–11940, 2018, doi: 10.1016/j.matpr.2018.02.167.

[12] X. Wu, X. Zhao, J. Chen, Z. Zhang, and C. Wu, “Simulation of the influence of welding parameters on weld pool behavior during a TIG-MIG hybrid welding process,” *J. Manuf. Process.*, vol. 79, no. December 2021, pp. 460–475, 2022, doi: 10.1016/j.jmapro.2022.05.007.

[13] P. Kumar, A. Nath, S. Chetan, K. Hirwani, and M. M. A. Saravanan, “Effect of welding current in TIG welding 304L steel on temperature distribution , microstructure and mechanical properties,” *J. Brazilian Soc. Mech. Sci. Eng.*, vol. 43, no. 7, pp. 1–20, 2021, doi: 10.1007/s40430-021-03082-6.

[14] A. Ebrahimpour, S. Salami, and T. Saeid, “Finite element investigation on the effect of arc configuration and torch angle on heat distribution in TIG - MIG hybrid welding of DSS,” pp. 2495–2509, 2022.

[15] R. Zong, J. Chen, and C. Wu, “A comparison of TIG-MIG hybrid welding with conventional MIG welding in the behaviors of arc , droplet and weld pool,” *J. Mater. Process. Tech.*, vol. 270, no. March, pp. 345–355, 2019, doi: 10.1016/j.jmatprotec.2019.03.003.

[16] M. Z. Siddiqi, “Finite Element Simulation of Weld Bead Geometry and Temperature Distribution during GTA Welding of Modified 9Cr-1Mo Steel and Experimental Validation,” *J. Manuf. Sci. Prod.*, vol. 14, no. 4, pp. 195–207, 2015, doi: 10.1515/jmsp-2014-0006.

[17] L. Chen, G. Mi, X. Zhang, and C. Wang, “Numerical and experimental investigation on microstructure and residual stress of multi-pass hybrid laser-arc welded 316L steel,” *Mater. Des.*, vol. 168, p. 107653, 2019, doi: 10.1016/j.matdes.2019.107653.

[18] A. Ermakova, A. Mehmanparast, S. Ganguly, J. Razavi, and F. Berto, “Fatigue Crack behaviour of wire and arc additively manufactured ER70S-6 low carbon steel components,” *Int. J. Fract.*, pp. 47–59, 2022.

[19] B. Das, B. Panda, and U. Dixit, “Microstructure and Mechanical Properties of ER70S-6 Alloy Cladding on Aluminum Using a Cold Metal Transfer Process,” *J. Mater. Eng. Perform.*, vol. 1, pp. 239–244, 2012.

[20] T. Ron, G. K. Levy, O. Dolev, A. Leon, A. Shirizly, and E. Aghion, “The effect of microstructural imperfections on corrosion fatigue of additively manufactured ER70S-6 alloy produced by wire arc deposition,” *Metals (Basel).*, vol. 10, no. 1, 2020, doi: 10.3390/met10010098.

[21] S. B. BROWN and H. SONG, “Implications of Three-Dimensional Numerica

Simulations of Welding of Large Structures," *Weld. Res. Suppl.*, vol. 71, no. 2, pp. 55s-62s, 1992.

[22] M. M. Mahapatra, G. L. Datta, B. Pradhan, and N. R. Mandal, "Three-dimensional finite element analysis to predict the effects of SAW process parameters on temperature distribution and angular distortions in single-pass butt joints with top and bottom reinforcements," *Int. J. Press. Vessel. Pip.*, vol. 83, pp. 721–729, 2006, doi: 10.1016/j.ijpvp.2006.07.011.

[23] "ASTM International, ASTM E384-17, Standard Test Method for Micro Indentation Hardness of Materials. West Conshohocken, PA: 2017."

[24] J. H. Lee, S. H. Park, H. S. Kwon, G. S. Kim, and C. S. Lee, "Laser, tungsten inert gas, and metal active gas welding of DP780 steel: Comparison of hardness, tensile properties and fatigue resistance," *Mater. Des.*, vol. 64, pp. 559–565, 2014, doi: 10.1016/j.matdes.2014.07.065.

[25] O. S. Sahasrabudhe and D. N. Raut, "Benchmarking of Hybrid TIG-MAG Arc Welding for Mild Steel," *Trans. Indian Inst. Met.*, vol. 72, no. 3, pp. 801–810, 2019, doi: 10.1007/s12666-018-1536-0.

[26] U. N. Khan, S. K. Rajput, V. Gupta, V. Verma, and T. Soota, "To study mechanical properties and microstructures of MIG welded high strength low alloy steel," in *Materials Today: Proceedings*, 2019, vol. 18, pp. 2550–2555. doi: 10.1016/j.matpr.2019.07.112.

[27] N. Yazdian, M. Mohammadpour, F. Kong, and R. Kovacevic, "Hybrid laser / arc girth welding of 304L stainless steel tubes , part 1 – Pore mitigation , thermal analysis and mechanical properties," *Int. J. Press. Vessel. Pip.*, vol. 163, pp. 75–93, 2018, doi: 10.1016/j.ijpvp.2018.05.003.

[28] G. F. Sun *et al.*, "Numerical and experimental investigation of thermal field and residual stress in laser-MIG hybrid welded NV E690 steel plates," *J. Manuf. Process.*, vol. 34, no. June, pp. 106–120, 2018, doi: 10.1016/j.jmapro.2018.05.023.

[29] A. J. R. Loureiro, "Effect of heat input on plastic deformation of undermatched welds," *J. Mater. Process. Technol.*, vol. 128, no. 1–3, pp. 240–249, 2002, doi: 10.1016/S0924-0136(02)00457-0.